Inorg. Chem. **2003**, *42*, 986–996

Structural and Physical Properties of the Ferromagnetic Tris-Dithiooxalato Compounds, $A[M^{II}Cr^{III}(C_2S_2O_2)_3]$, with $A^+ = N(n\text{-}C_nH_{2n+1})_4^+$ (n = 3–5) and $P(C_6H_5)_4^+$ and M^{II} = Mn, Fe, Co, and Ni

Justin M. Bradley,[†] Simon G. Carling,[†] Dirk Visser,[‡,§,||] Peter Day,*[,†] Dimitri Hautot,[†] and Gary J. Long*[,⊥]

Davy Faraday Research Laboratory, The Royal Institution of Great Britain, 21 Albemarle Street, London W1S 4BS, U.K., Department of Physics, Warwick University, Coventry CV4 7AL, U.K., NWO-EW, ISIS Facility, Rutherford Appleton Laboratory, Chilton, Didcot OX110QX, U.K., IRI, TU-Delft, Mekelweg 15, 2629JB Delft, The Netherlands, and Department of Chemistry, University of Missouri—Rolla, Rolla, Missouri 65409-0010

Received April 29, 2002

The structural and magnetic properties of the tris-dithiooxalato salts, $A[M^{II}Cr(C_2S_2O_2)_3]$, have been investigated with $A^+ = PPh_4^+$, $N(n\text{-}C_nH_{2n+1})_4^+$, with n = 3–5, where M^{II} is Mn, Fe, Co, and Ni. With the exception of $A[MnCr(C_2S_2O_2)_3]$, all the salts are ferromagnets with Curie temperatures, T_c, between 5 and 16 K. In contrast to the corresponding oxalates which are ferromagnetic, the $A[MnCr(C_2S_2O_2)_3]$ compounds are paramagnetic above 2 K. Powder neutron diffraction studies of d_{20}-$PPh_4[FeCr(C_2S_2O_2)_3]$ indicate that no structural phase transitions occur between 2.4 and 285 K and that the coefficient of linear expansion is four times larger for the *c*-axis than for the *a*-axis. The crystal structure refined from powder neutron diffraction data confirms the honeycomb layer arrangement observed in the related bimetallic tris-oxalate salts. The Mössbauer spectra reveal that the iron(II) in $PPh_4[FeCr(C_2S_2O_2)_3]$ is coordinated mainly to six oxygen atoms of the dithiooxalato ligand but with a minor component of sulfur coordination that increases with aging of the sample; the iron(II) is high-spin in both cases. Powder neutron diffraction profiles of d_{20}-$PPh_4[FeCr(C_2S_2O_2)_3]$ below T_c show magnetic intensity with a $q = 0$ propagation vector, confirming the presence of ferromagnetic order.

Introduction

Because of their unusual magnetic properties there has been much interest in the extensive series of bimetallic tris-oxalato salts with the general formula $A[MM'(C_2O_4)_3]$, where A^+ is an organic cation and M and M′ are, respectively, divalent and trivalent transition metal ions.[1−3] The metal ions, bridged by the ambidentate $C_2O_4^{2-}$ ligand, form hexagonal honeycomb layers interleaved by the organic cations, whose side chains both penetrate the hexagonal cavities within the layers and fill the space between them. The chief interest in these compounds is in both their zero-field and field-cooled magnetic behavior which may be either ferrimagnetic or ferromagnetic depending on M and M′ and, in the case of the Fe(II,III) compounds, may be remarkably dependent upon the organic cation.[4] In contrast, the corresponding dithiooxalato compounds are relatively unstudied, although the ability of $[C_2S_2O_2]^{2-}$ to transmit magnetic exchange interactions has been verified through the synthesis and study of discrete dimeric compounds.[5]

Tetra-*n*-propylammonium salts containing Cr^{III} and several divalent 3d transition metal ions have been reported[6] to be ferromagnetic. Hence, the aim of this work is to extend the

* Authors to whom correspondence should be addressed. E-mail: pday@ri.ac.uk (P.D.); glong@umr.edu (G.J.L.).
† The Royal Institution of Great Britain.
‡ Warwick University.
§ Rutherford Appleton Laboratory.
|| TU-Delft.
⊥ University of Missouri—Rolla.

(1) Tamazaki, H.; Zhong, Z.; Matsumoto, N.; Kida, S.; Koikawa, M.; Aihiwa, N.; Hashimoto, Y.; Okawa, H. *J. Am. Chem. Soc.* **1992**, *114*, 6974.
(2) Decurtins, S.; Schmalle, H. W.; Oswald, R.; Linden, A.; Ensling, J.; Gütlich, P.; Hauser, A. *Inorg. Chim. Acta* **1994**, *216*, 65.
(3) Mathonière, C.; Nuttall, C. J.; Carling, S. G.; Day, P. *Inorg. Chem.* **1996**, *35*, 1201.
(4) Mathonière, C.; Carling, S. G.; Dou, Y.; Day, P. *J. Chem. Soc., Chem. Commun.* **1994**, 1554.
(5) Mitsumi, M.; Okawa, H.; Sikiyama, H.; Ohba, M.; Matsumoto, N.; Kurisuki, T.; Wakita, H. *J. Chem. Soc., Dalton Trans.* **1993**, 2991.
(6) Okawa, H.; Mitsuni, M.; Ohba, M.; Kodera, M.; Matsumoto, N. *Bull. Chem. Soc. Jpn.* **1994**, *67*, 2139.

10.1021/ic020302x CCC: $25.00
Published on Web 01/22/2003

Table 1. Elemental Analyses of $A[M^{II}Cr(C_2S_2O_2)_3]$

A^+	M^{II}		% C	% H	% N or P	% S	% M^{II}	% Cr^{III}
$N(n\text{-}C_3H_7)_4^+$	Mn^{II}	calcd	33.03	4.32	2.15	29.38	8.41	7.95
		obsd	32.70	4.51	2.17	27.01	8.28	7.81
	Fe^{II}	calcd	33.03	4.31	2.14	29.30	8.53	7.93
		obsd	32.74	4.56	2.23	26.73	8.30	7.85
	Ni^{II}	calcd	32.96	4.30	2.14	29.25	8.95	7.92
		obsd	32.00	4.45	2.20	27.08	8.61	7.80
	Co^{II}	calcd	32.91	4.30	2.13	29.20	8.97	7.91
		obsd	31.78	4.41	2.19	26.98	8.59	7.78
$N(n\text{-}C_4H_9)_4^+$	Mn^{II}	calcd	37.27	5.11	1.98	27.06	7.75	7.33
		obsd	36.07	5.25	2.07	25.43	7.34	7.29
	Fe^{II}	calcd	37.22	5.11	1.97	27.02	7.87	7.32
		obsd	36.65	5.14	2.05	24.99	7.44	7.13
	Ni^{II}	calcd	37.11	5.10	1.97	26.94	8.25	7.30
		obsd	36.42	5.15	2.06	25.06	8.02	7.10
	Co^{II}	calcd	37.06	5.09	1.96	26.91	8.27	7.29
		obsd	36.33	5.20	2.08	25.24	7.94	7.13
$N(n\text{-}C_5H_{11})_4^+$	Fe^{II}	calcd	40.73	5.79	1.83	25.04	7.29	6.78
		obsd	38.77	5.53	1.90	22.74	7.11	6.63
PPh_4^+	Fe^{II}	calcd	44.62	2.50	3.84	23.78	6.92	6.44
		obsd	41.66	2.47	4.18	20.44	7.24	5.96
	Ni^{II}	calcd	44.50	2.49	3.83	23.72	7.26	6.42
		obsd	42.45	2.41	4.07	21.22	7.43	5.99
	Co^{II}	calcd	44.45	2.49	3.82	23.69	7.28	6.41
		obsd	43.07	2.40	4.05	20.76	7.41	5.84

range of organic cations studied, to determine whether the structures are indeed analogous to those of the corresponding oxalates, to examine the low-temperature magnetization, and, in the case of the PPh_4^+ salt which can be readily deuterated, to confirm by powder neutron diffraction studies whether the ordered magnetic structure is ferromagnetic.

Experimental Section

Synthesis. Starting materials were obtained from Aldrich and were of 99.9% or better purity. All reagents and solvents were used as purchased unless otherwise stated.

The dipotassium *cis*-dithiooxalate salt, $K_2C_2S_2O_2$, was prepared through the reaction of potassium metal with H_2S in ethanol to produce KHS.[7] To this was added the diphenyl-thio-ester obtained from oxalyl chloride and thiophenol to produce $K_2C_2S_2O_2$. The product was washed with ethanol to remove excess KHS, dried overnight, and further purified by mixed-solvent recrystallization from a 1:3:9 mixture of water, methanol, and diethyl ether, to produce a white solid in 35% yield. Elemental anal. Measd (calcd): C 12.20 (12.11), S 30.77 (32.29). The low sulfur content is due to the release of H_2S on exposure to air.

To prepare the bimetallic dithiooxalate salts, $A[M^{II}Cr(C_2S_2O_2)_3]$, 0.26 g (1 mmol) of $CrCl_3{\cdot}6H_2O$ was dissolved in 25 mL of degassed water, 0.5 g (3 mmol) of $K_2C_2S_2O_2$ was added, and the solution was heated for 30 min at 60 °C until it turned reddish-brown. Next, 1 mmol of $MCl_2{\cdot}xH_2O$ was added and the solution heated at 80°C for an additional 20 min before addition of 1 mmol of ABr, where A^+ is the appropriate organic cation. The solution was then maintained at 80°C until the precipitation of $A[M^{II}Cr(C_2S_2O_2)_3]$ was complete.[6] The product was then cooled, filtered, and washed with successive aliquots of water, methanol, and diethyl ether; the yield in all cases was close to 100%.

The results of the elemental analysis for all the compounds studied herein are given in Table 1. The carbon content is slightly low in all cases whereas phosphorus in the PPh_4 salts is high. Likewise the sulfur content is low in all cases, as in $K_2C_2S_2O_2$. The bimetallic dithiooxalate salts are air sensitive. Small quantities of S_8 are detected in their X-ray diffraction profiles.

(7) Jones, H. O.; Tasker, H. S. *J. Chem. Soc.* **1909**, 1904.

Synthesis of d_{20}-$PPh_4[MFe(C_2S_2O_2)_3]$. $Fe(NO_3)_3{\cdot}9H_2O$ (3.43 g, 0.0085 mol) was dissolved in 250 mL of degassed water, then 5 g (0.025 mol) of $K_2C_2S_2O_2$ was added, and the resulting deep purple solution was stirred for approximately 20 min. Next, 2.78 g (0.01 mol) of $FeSO_4{\cdot}5H_2O$ or 2.97 g (0.015 mol) of $MnCl_2{\cdot}6H_2O$ was added to the solution of $K_3Fe(C_2S_2O_2)_3$. After stirring for a further 30 min the solution was filtered to remove any S_8 and FeS precipitates. Then 3.4 g (0.008 mol) of d_{20}-PPh_4Br was added and the solution stirred overnight under a nitrogen atmosphere. The product was then collected by filtration, washed with aliquots of water, methanol, and diethyl ether, and then dried under vacuum to give 5 g of product with a yield in each case of ca. 75%.

X-ray Diffraction. Powder X-ray diffraction profiles were obtained on a Siemens D500 flat plate diffractometer fitted with a primary monochromator to remove all but the Cu $K\alpha_1$ radiation. Rapid scans, used for phase identification, were obtained at 2θ values between 5° and 45° with a step of 0.02°, a counting time of 1 s per data point, and collimation slits limiting the beam divergence to 1°. Slow scans, used to extract the unit cell parameters and to check the phase purity, were obtained over the same angular range and step size but with a counting time of 20 s per data point and with collimation slits limiting the beam divergence to 0.3°.

High-resolution powder X-ray diffraction data were collected on beam line BM16 at the ESRF, Grenoble, France. Ground samples were sealed inside glass capillaries of 1 mm internal diameter and 1.5−2 cm length. The capillary was mounted on an independent spinning motor on the axis of the diffractometer in order to reduce the effects of crystallite orientation. The sample was placed in a helium cryostat operating between 2 K and room temperature. The energy of the incident X-rays was tunable between 5 and 40 keV by using a double Si (111) monochromator with sagittal focusing on the second Si crystal. The wavelength used was 0.800615 Å, a value which is both well separated from the absorption edges of any of the elements in the samples and in the region of minimal instrumental broadening of the peak width; the full peak width at half-maximum was approximately 0.06° in 2θ. Data were collected as continuous scans in order to eliminate the step scan dead time. Diffraction data were recorded between 4° and 38° in 2θ at room temperature and 12 K. Below 13° 2θ the scan speed was 0.6°/min, between 13° and 30° 2θ 0.4°/min, and 0.2°/min above 30° 2θ. In addition rapid scans were obtained between 4.5° and 10° in 2θ at a scan rate of 0.6°/min while cooling from room temperature to 2 K. The data were subsequently binned to the desired step size and normalized.

Individual peaks and groups of peaks were fitted to pseudo-Voigt functions with the XFIT program. The resulting peak positions were then used with the TREOR90 autoindexing program to index the reflections and estimate the unit cell parameters. The latter were then used as the starting point for a LeBail fit with the GSAS profile fitting program.[8]

Neutron Diffraction. Powder neutron diffraction studies were carried out on d_{20}-$PPh_4[FeCr(C_2S_2O_2)_3]$ placed in vanadium sample holders, in cryostats enabling temperature variation between 1.5 and 300 K. Data were recorded on the D2B diffractometer at the ILL, Grenoble, France, at a constant wavelength of 2.40 Å with no collimation in order to maximize the count rate. Peak widths at this resolution were still sample determined. Diffraction profiles were constructed from 50 data blocks (100000 monitor counts) with a step size of 0.05°.

Time-of-flight neutron diffraction measurements were performed at the ISIS pulsed neutron source at the Rutherford Appleton

(8) Larson, A. C.; Von Dreele, R. B. *Los Alamos Natl. Lab, [Rep.] LA (U.S.)* **1986**, *LAUR 86-748*.

Laboratory, Chilton, U.K. Data were collected on the GEM diffractometer at room temperature and at selected temperatures between 2 and 10 K. Each profile was collected for a monitor count of 200 μA. Additional profiles were measured at 2 and 20 K on the OSIRIS spectrometer, operating in diffraction mode. Several separate, overlapping blocks were measured to cover a wide range of *d* spacings with the monitor count per block varying from 30 μA at large *d* spacing to 67.5 μA at short *d* spacing.

DC Magnetization. DC magnetization was measured with a Quantum Design MPMS-7 SQUID magnetometer with longitudinal detector coils. A helium-cooled superconducting magnet permitted the application of a DC magnetic field of between −7 and 7 T between 1.8 and 400 K. The powder samples, whose mass was obtained with a precision of ±0.001 mg, were placed in gelatin capsules inserted into plastic straws and secured in the magnetometer with empty gelatin capsules surrounded by nonmagnetic tape.

Initial magnetic characterization was carried out at 0.01 T by measuring the field-cooled magnetization between 2 and 300 K and the zero-field-cooled magnetization between 5 and 50 K. To compensate for the remnant field of the superconducting magnet, small compensating fields were applied at 100 K until the response from the coils was less than 10^{-7} emu. The sample was then cooled to 5 K in zero field before a field of 0.01 T was applied. The temperature was increased to 50 K while the response was measured at regular temperature intervals. The temperature was then increased to 100 K to ensure that the samples were paramagnetic before the field-cooled measurements were commenced. The 0.01 T field was maintained during cooling to 2 K, with a pause for temperature stabilization at 5 K, and the response was again measured during warming from 2 to 300 K. All measurements were corrected for the diamagnetic susceptibility of the sample by using Pascal's constants.

Mössbauer Spectroscopy. The Mössbauer spectra were measured at 78 and 295 K on a constant-acceleration spectrometer which utilized a room temperature rhodium matrix cobalt-57 source and was calibrated at room temperature with α-iron foil. The spectra were fit with three symmetric quadrupole doublets, and the estimated absolute errors are ±0.01 mm/s for the isomer shifts, quadrupole splittings, and line widths and ±0.5% for the relative spectral areas.

Results and Discussion

Structural Characterization. The powder X-ray diffraction profiles of all of the $N(n\text{-}C_3H_7)_4[M^{II}Cr(C_2S_2O_2)_3]$ compounds have been indexed in the hexagonal $P6_3$ space group. For the compounds with $N(n\text{-}C_4H_9)_4^+$, $N(n\text{-}C_5H_{11})_4^+$, and PPh_4^+, the powder diffraction profiles suggests the hexagonal $P6_3$ space group. In these compounds the position of the (002) reflection provides an estimate of the *c*-axis lattice parameter, and, in some cases, the (100) and (010) reflections can also be used to obtain the *a*-axis lattice parameter. A comparison of the resulting unit cell parameters with those of the corresponding oxalate compounds suggests that the direction of stacking of the layers is along the crystallographic *c*-axis, and the lattice parameters suggest that the stacking sequence is A−B in all cases. This sequence differs from the intergrowth of A−B and A−B−C sequences observed in the corresponding oxalate compounds.[9,10] No reflections with *d* spacings of less than 1 Å are observed, indicating poorly developed long-range order.

Table 2. Lattice Parameters of $A[M^{II}Cr(C_2S_2O_2)_3]$

M^{II}	A^+	*a*, Å	*c*/2, Å
Mn^{II}	$N(n\text{-}C_3H_7)_4^+$	10.25[a]	7.87[a]
	$N(n\text{-}C_4H_9)_4^+$	10.86[b]	8.9[c]
Fe^{II}	$N(n\text{-}C_3H_7)_4^+$	10.10[a]	7.99[a]
	$N(n\text{-}C_4H_9)_4^+$		9.01[c]
	$N(n\text{-}C_5H_{11})_4^+$		9.50[c]
	PPh_4^+	10.17[a]	9.13[a]
Co^{II}	$N(n\text{-}C_3H_7)_4^+$	10.17[b]	8.13[c]
	$N(n\text{-}C_4H_9)_4^+$	10.60[b]	9.95[c]
	PPh_4^+	10.09[b]	9.27[c]
Ni^{II}	$N(n\text{-}C_3H_7)_4^+$	10.60[b]	8.05[c]
	$N(n\text{-}C_4H_9)_4^+$	10.52[b]	9.90[c]
	PPh_4^+	10.42[b]	9.30[c]

[a] Refined values obtained using the LeBail method (ref 8). [b] Calculated from the position of the (100) peak. [c] Calculated from the position of the (002) peak.

The unit cell parameters were obtained either with the LeBail method, which uses the entire diffraction profile, or from the (001) and (100) reflections; the results are given in Table 2. As expected, the *c*-axis increases with *n* in C_nH_{2n+1}, corresponding to an increase in the interlayer separation, as the cations interleave the metal−organic sheets. The *c*-axis parameter equates to the interlayer separation in the A−B stacking sequence compared with the corresponding oxalates, in which the interlayer separations are *c*/6 for the *R*3*c* and $P6_5$ space groups or *c*/2 for the $C222_1$ space group.[9,10] There is an increase of approximately 10% in the *a*-axis and a small decrease in the interlayer separation from the oxalate to dithiooxalate compounds.[3] The former increase results from the larger ionic radius of sulfur as compared with oxygen, and the latter decrease results from the larger hexagonal holes in the honeycomb lattice, which permit a greater penetration of the alkyl side chains into the anion layers.

In spite of the limited range of compounds, it is clear that the $A[FeCr(C_2S_2O_2)_3]$ series shows a variation in interlayer separation with increasing alkyl chain length that is opposite to that of the oxalates. With both $N(n\text{-}C_nH_{2n+1})_4^+$, with $n = 3-5$, and $PPh_3(n\text{-}C_nH_{2n+1})^+$, with $n = 3-7$, the oxalates show[3,10] the classic alternation in layer separation, i.e., an increase from n_{even} to n_{odd} which is much greater than the increase from n_{odd} to n_{even}. This results from the conformation of the CH_2 which is added to the alkyl chain as *n* increases. In contrast, in $N(n\text{-}C_nH_{2n+1})[FeCr(C_2S_2O_2)_3]$ the interlayer separation increases more from $n = 3$ to 4 than $n = 4$ to 5. Unfortunately, no compounds with $n = 2$ or 6 can be isolated. Most probably the unusual dependence of the interlayer separation on the alkyl chain length results from a change in conformation of the cation in the interlamellar space, such as that observed[11] in the oxalate series as *n* increases from 4 to 5. Nevertheless, the broad similarity between the interlayer separations in the dithiooxalate and oxalate-based compounds suggests that overall the alkyl chains adopt similar orientations in the interlamellar space.

(9) Nuttall, C. J.; Day, P. *J. Solid State Chem.* **1999**, *147*, 3.
(10) Watts, I. D.; Carling, S. G.; Day, P. *J. Chem. Soc., Dalton Trans.* **2002**, 1429.
(11) Carling, S. G.; Mathonière, C.; Day, P.; Malik K. M. A.; Hursthouse, M. B. *J. Chem. Soc., Dalton Trans.* **1996**, 1839.

Table 3. Lattice Parameters of $N(n\text{-}C_3H_7)_4[M^{II}Cr(C_2S_2O_2)_3]$

M^{II}	a, Å	$c/2$, Å	χ^2	R_{WP}, %
Fe^{II}	10.169[a]	15.9797[a]	3.869	8.57
	10.10[b]	15.98[b]	1.453	11.63
Mn^{II}	10.2455[a]	15.7472[a]	2.9874	8.24
	10.25[b]	15.74[b]	0.8208	11.63

[a] Data obtained from BM16 at the ESRF. [b] Data obtained on a D500 X-ray diffractometer.

The bulkier PPh_4^+ cation causes an increase in the *c*-axis in $PPh_4[M^{II}Cr(C_2S_2O_2)_3]$, when M^{II} is Fe, Co, or Ni, as compared to the $N(n\text{-}C_3H_7)_4^+$ compounds. Furthermore, in the $N(n\text{-}C_3H_7)_4$ series the *c*-axis increases from Mn to Co. As in the corresponding oxalate compounds, this increase correlates with a decrease in the M^{II} ionic radius, resulting in a reduction in the size of the hexagonal cavities within the anion layers. As a consequence, the alkyl side chains do not penetrate as far into the pores and the interlayer separation increases.[3] In summary, the powder X-ray diffraction studies indicate that the extended two-dimensional honeycomb network structure forms for all combinations of M^{II} and Cr^{III} and organic cations examined. This conclusion conflicts with a previous study which stated[6] that such compounds do not form when M^{II} is Mn^{II} and for cations other than $N(n\text{-}C_3H_7)_4^+$.

High-resolution powder synchrotron X-ray diffraction profiles of $N(n\text{-}C_3H_7)_4[FeCr(C_2S_2O_2)_3]$ and $N(n\text{-}C_3H_7)_4[MnCr(C_2S_2O_2)_3]$ reveal additional weak reflections not evident in those obtained with laboratory X-ray sources. LeBail fitting of these profiles reveals two distinct phases, one with the characteristic broad reflections of the dithiooxalate compounds and a second with sharper but much less intense reflections. The former reflections index with the hexagonal $P6_3$ space group whereas the weaker reflections may be indexed as S_8, an impurity.[12] The resulting best fit unit cell parameters for $N(n\text{-}C_3H_7)_4[FeCr(C_2S_2O_2)_3]$ and $N(n\text{-}C_3H_7)_4[MnCr(C_2S_2O_2)_3]$ are given in Table 3, and the diffraction profile for the former compound, along with its LeBail fit with a Lorentzian peak shape, is shown in Figure 1.

The neutron diffraction profiles of $d_{20}\text{-}PPh_4[FeCr(C_2S_2O_2)_3]$ were indexed in the hexagonal $P6_3$ space group. The structure was found to be independent of temperature between 1.5 and 300 K, and the high-resolution profiles, measured at 1.5, 10, and 50 K, were identical except for the effects of thermal expansion; the profile obtained at 50 K and its fit, with $a = 10.103(2)$ Å and $c = 17.998(4)$ Å, are shown in Figure 2. The crystal structure refined from the powder neutron diffraction data is almost identical to that of $PPh_4[MnFe(C_2S_2O_2)_3]$ refined from unpublished synchrotron X-ray diffraction results. Refinement of the structure by the Rietveld method is difficult because the large unit cell of ca. 1600 $Å^3$ contains 130 atoms. In the $P6_3$ space group, the positional parameters of 31 atoms are required to describe the unit cell content. The problem is further exacerbated by poor crystallinity. Below 50 K the background of the neutron diffraction profiles shows no variation with temperature. Consequently,

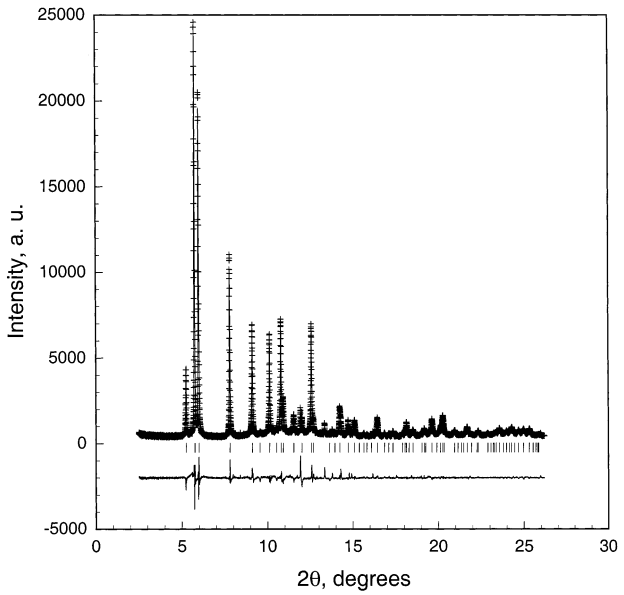

Figure 1. The powder X-ray diffraction profile of $N(n\text{-}C_3H_7)_4[FeCr(C_2S_2O_2)_3]$ obtained at 300 K and its LeBail fit with a Lorentzian peak shape. The fit residuals are shown at the bottom of the figure.

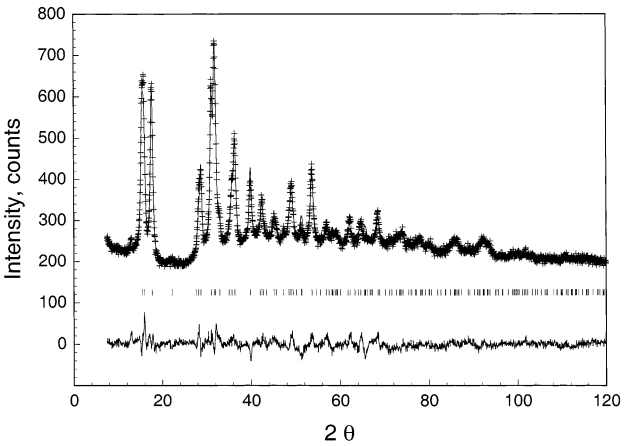

Figure 2. The powder neutron diffraction profile of $d_{20}\text{-}PPh_4[FeCr(C_2S_2O_2)_3]$ obtained at 50 K on D2B and its Rietveld profile. The positions of the various reflections are shown as small bars, and the fit residuals are shown at the bottom of the figure.

below 50 K, the disordered diffuse contribution must be due to the static disorder. One P−C bond of the PPh_4^+ cation is oriented along a C_3 axis in the $P6_3$ space group, and the corresponding phenyl ring was therefore modeled with three orientations, each $^1/_3$ occupied and at 120° to each other. This ring comprises the atoms labeled C11 to C16 and H12 to H16, see below. No particular angle relative to the *a*-axis resulted in a substantially improved fit.

The Rietveld refinement was performed on the 50 K data using the FULLPROF[13] code. The lattice parameters and parameters indicating the quality of the fit are listed in Table 4, and the measured and calculated profiles are shown in Figure 2. To obtain a refinement model the structure was simulated by two independent rigid bodies defined by the $C_2S_2O_2$ group and the $d_{20}\text{-}PPh_4$ group. Each group was defined by various bond lengths, bond angles, position, and

(12) Wyckoff, R. W. G. *Crystal Structures*, 2nd ed.; Interscience: New York, 1963; Vol. 1, p 33.

(13) Rodriguez-Carvajal, J. *FULLPROF: Reference Guide to the Program 3.2*; CEA-CNRS: Paris, 1997.

Table 4. Characteristics of the Rietveld Fit of the Neutron Diffraction Profile of d_{20}-$PPh_4[FeCr(C_2S_2O_2)_3]$

a, Å	10.101(2)
c, Å	18.001(4)
V, Å^3	1590.6(6)
λ, Å	2.40
T, K	50
χ^2	2.89
R_{WP}	14.4
R_P	13.7
R_e	8.46
space group	$P6_3$

Table 5. Selected Bond Distances and Bond Angles in $PPh_4[FeCr(C_2S_2O_2)_3]$ at 50 K

Dithiooxalate Rigid Body			
	distance, Å		angle, deg
Fe−O1	2.09(5)	O1−Fe−O1	88(2)
Fe−O2	2.09(5)	O1−Fe−O2	92(2)
Cr−S1	2.1(1)	S1−Cr−S1	100(4)
Cr−S1	2.1(1)	S1−Cr−S2	101(4)
C1−O1	1.21(6)		
C2−O2	1.29(6)	C11−P−C13	154(6)
C1−C2	1.55(4)	C13−P−C13	85(6)
C1−S1	1.6(1)		
C2−S2	1.6(1)		

PPh_4 Rigid Body			
	distance, Å		distance, Å
P−C11	1.7(1)	P−C13	1.6(1)
C11−C21	1.3(1)	C13−C23	1.39(6)
C21−C31	1.6(1)	C23−C33	1.38(4)
C31−C41	1.3(1)	C33−C43	1.25(8)
C41−C51	1.3(1)	C43−C53	1.41(5)
C51−C61	1.3(1)	C53−C63	1.32(4)
C61−C11	1.4(1)	C63−C13	1.31(7)
C21−D21	1.0(1)	C23−D23	0.96(7)
C31−D31	1.0(1)	C33−D33	0.95(6)
C41−D41	1.0(1)	C43−D43	0.96(4)
C51−D51	1.0(1)	C53−D53	0.96(5)
C61−D61	1.0(1)	C63−D63	0.95(7)

rotation angles, which were manually refined until the best χ^2 and R_{WP} were reached and gave good values for the positional parameters. This model was then further refined, as independent atoms, to give positional parameters, supplied as Supporting Information. The final refinement allowed for all coordinates of all atoms to vary independently with the exception of a few constraints. For example, in the $C_2S_2O_2$ group atoms of the same element were constrained to move together symmetrically so that, e.g., both Fe−O distances remained equal. The R_{WP} of the fit is fairly high, in part due to the disorder which is also reflected in the error bars on the positional parameters and the bond distances. Selected bond distances and angles are also reported in Table 5. The refined structure, illustrated in Figure 3, confirms the presence of a honeycomb structure just as in the oxalates, as well as the presence of organic cations between the layers of metals chelated by dithiooxalate ligands.

To examine the variation of the structure with temperature, powder neutron diffraction profiles of d_{20}-$PPh_4[FeCr(C_2S_2O_2)_3]$ were measured at 0.5, 1, and 10 K intervals between 2.4 and 10 K, 10 and 20 K, and 20 and 285 K, respectively, using the high-intensity D20 diffractometer. The profiles were fit with a pseudo-Voigt line profile by using FULLPROF[13] and the structural model refined from the high-resolution profile measured on D2B at 50 K. The a-axis and

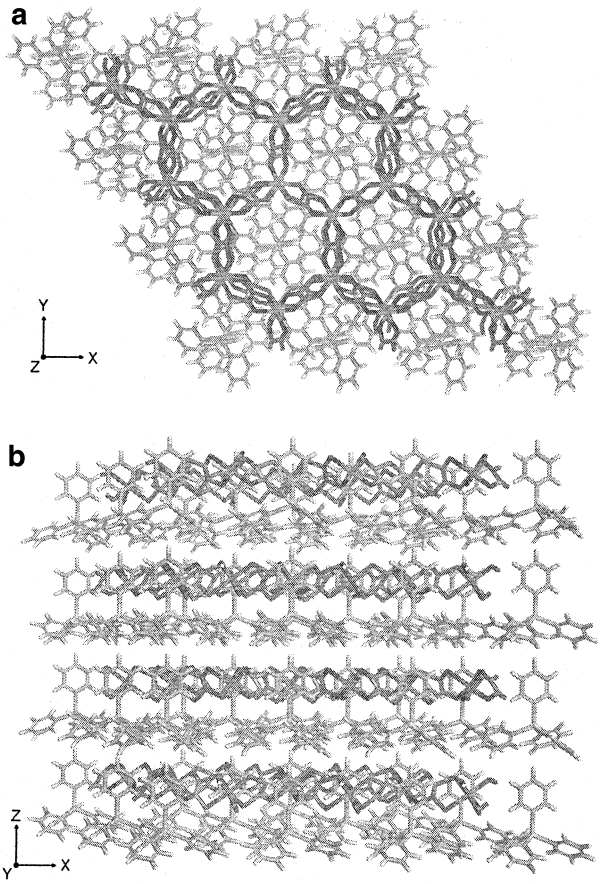

Figure 3. (a) Structure of d_{20}-$PPh_4[FeCr(C_2S_2O_2)_3]$ viewed along 001. (b) Structure of d_{20}-$PPh_4[FeCr(C_2S_2O_2)_3]$ viewed perpendicular to 001.

c-axis unit cell parameters were obtained with a precision of ca. ±0.003 and ±0.006 Å, respectively, and the temperature dependence of the a- and c-lattice parameters, see Figure 4, was fit with the expressions

$$a = \Delta a_0\left[\coth\left(\frac{h\nu_a}{2kT}\right) - 1\right] + a_0 \quad (1)$$

and

$$c = \Delta c_0\left[\coth\left(\frac{h\nu_c}{2kT}\right) - 1\right] + c_0 \quad (2)$$

where a_0 and c_0 are the zero Kelvin lattice parameters, Δa_0 and Δc_0 are the differences between the observed lattice parameters and their values obtained from a linear extrapolation from higher temperatures, and ν_a and ν_c are mean lattice phonon frequencies in the a and c directions. In the fits shown in Figure 4, a_0, c_0, Δa_0, Δc_0, ν_a, and ν_c are adjustable parameters. Equations 1 and 2 were obtained for the specific case of the lattice expansion and are derived from the Einstein model[14] for the lattice heat capacity.[15,16] Comparable

(14) Kittel, C. *Introduction to Solid State Physics*, 4th ed.; Wiley: New York, 1974.
(15) Touloukian, Y. S. *Thermal Expansion—Metallic Elements and Alloys*, Vol. 12: Thermal *Expansion—Nonmetallic Solids*; Plenum: New York, 1977.
(16) Touloukian, Y. S. *Thermophysical Properties of Matter, Vol. 13: Thermal Expansion—Nonmetallic Solids*; Plenum: New York, 1977.

equations modeling the temperature dependence of the coefficient of linear expansion based on the Debye model are described by Askerov and Cankurtaran.[17] The latter predicts a power law dependency at low temperature for the heat capacity but also for the linear coefficient of expansion α. However, in the present case, the temperature dependence of the lattice parameters does not follow a power law but is exponential as shown in Figure 4.

The Einstein model assumes a single mean phonon frequency, and the fit to eqs 1 and 2 gives lattice constants at 0 K of 10.108 and 18.016 Å for a_0 and c_0, respectively, and 0.021 and 0.095 Å for Δa_0 and Δc_0, respectively. The mean lattice phonon frequencies, ν_a and ν_c, were found to be 77.5 and 48.9 cm^{-1}. and the Einstein temperatures, θ, were 222 and 140 K, respectively, in good agreement with the Debye temperatures of 159 K in the low-temperature range and 100 K in the high-temperature range estimated from the Mössbauer spectrum of the related compound N(*n*-C_4H_7)[$FeFe(C_2O_4)_3$].[18] One reason why the Einstein model applies so successfully to d_{20}-PPh_4[$FeCr(C_2S_2O_2)_3$] is that, because of its layered nature, the phonon spectra along *a* and *c* are each dominated by a single frequency.

The unit cell volume, *V*, is obtained by substituting eqs 1 and 2 into the expression for the volume of a hexagonal unit cell, $V = (a^2c\sqrt{3})/2$. The complete expression for eq 3

$$V = \left[(a_0 - \Delta a_0)^2(c_0 - \Delta c_0) + \Delta c_0(a_0 - \Delta a_0)^2 \coth\left(\frac{h\nu_c}{2kT}\right) + \Delta c_0(a_0 - \Delta a_0)(c_0 - \Delta c_0) \coth\left(\frac{h\nu_a}{2kT}\right)\right]\frac{\sqrt{3}}{2} \quad (3)$$

contains additional terms all of which contain a product of at least two coth terms, terms which are small and contribute at most ±0.001% to the volume at 300 K.

The coefficient of linear expansion, α, is defined by the lattice parameter and its slope,

$$\alpha_a(T) = \frac{1}{a}\frac{da}{dT} \quad (4)$$

and from eq 1 we obtain

$$\alpha_a(T) = \frac{\Delta a_0 h\nu_a}{2kT^2} \frac{\operatorname{csch}^2\left(\frac{h\nu_a}{2kT}\right)}{\Delta a_0\left[\coth\left(\frac{h\nu_a}{2kT}\right) - 1\right] + a_0} \quad (5)$$

and, in the high-temperature limit, the product of *a* and α approaches a constant value,

$$\alpha_{a,HT}a = \frac{2\Delta a_0 k}{h\nu_a} \quad (6)$$

which is 1.89×10^{-4} and 1.36×10^{-3} Å/K for the *a*- and *c*-lattice parameters, respectively.

From the temperature dependence of the lattice parameters of d_{20}-PPh_4[$FeCr(C_2S_2O_2)_3$], the coefficients of linear expansion at high temperature are 18×10^{-6} and 76×10^{-6} K^{-1} along the *a*- and *c*-axes, respectively. The difference in these values reflects the different nature of the bonding in the two directions. The *a*-axis direction has an α which is similar to those of some metals such as copper for which α is 17×10^{-6} K^{-1}; most metals have $\alpha < 40 \times 10^{-6}$ K^{-1}.[15,16] Inorganic salts have room temperature coefficients of linear expansion which are typically between 25×10^{-6} and 40×10^{-6} K^{-1}, the values observed for $CaCO_3$ and NaCl, respectively.[15,16] Higher α values, in the range of 82×10^{-6} to 113×10^{-6} K^{-1}, are found in polymers such as polystyrene and polycarbonate.[15,16] The latter are similar to the α value observed for the *c*-axis, 76×10^{-6} K^{-1}, in d_{20}-PPh_4[$FeCr(C_2S_2O_2)_3$], suggesting that the bonding in this direction is weaker and comparable to that observed in polymers.

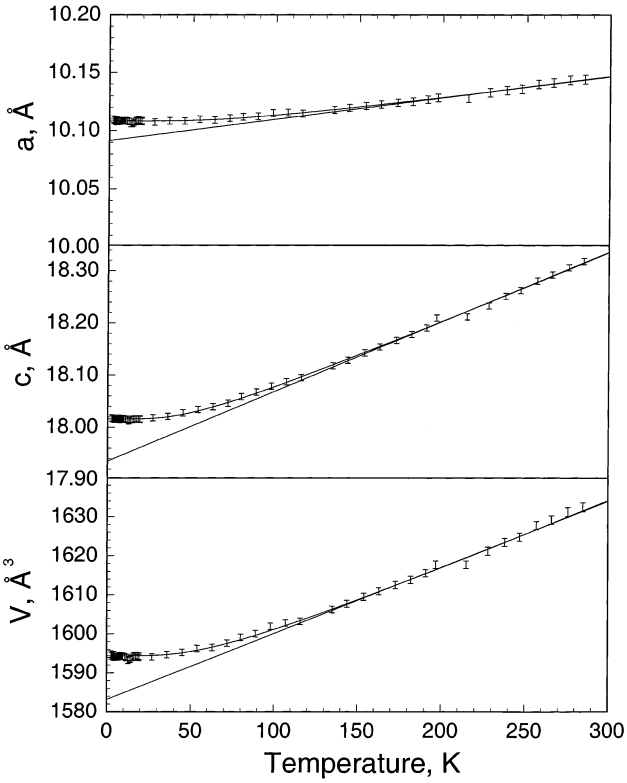

Figure 4. The temperature dependence of the lattice parameters and unit cell volume for d_{20}-PPh_4[$FeCr(C_2S_2O_2)_3$].

Both coefficients of linear expansion for d_{20}-PPh_4[$FeCr(C_2S_2O_2)_3$] are compatible with a stacking along the *c*-axis of a two-dimensional covalent bonding network in the basal plane. The temperature variation of the coefficient of linear expansion, $d\alpha/dT$, is complex, but may be solved numerically; it passes through a maximum, as shown in the inset to Figure 5. The variation in the coefficient of linear expansion is small but increases at lower temperature and reaches a maximum at 49 and 31 K for the *a*-axis and *c*-axis, respectively, see the inset to Figure 5. It is important to note that the expansion of the lattice is anisotropic; $d\alpha/dT$ is much smaller for the *a*-axis than for the *c*-axis.

Below the Curie temperature, powder neutron diffraction profiles of d_{20}-PPh_4[$FeCr(C_2S_2O_2)_3$] contain a small magnetic contribution with a propagation vector, **q**, of 0, i.e., all the

(17) Askerov, B. M.; Cankurtaran, M. *Phys. Status Solidi B* **1994**, *185*, 341.
(18) Iijima, S.; Mizutani, F. *Mol. Cryst. Liq. Cryst.* **1997**, *306*, 227.

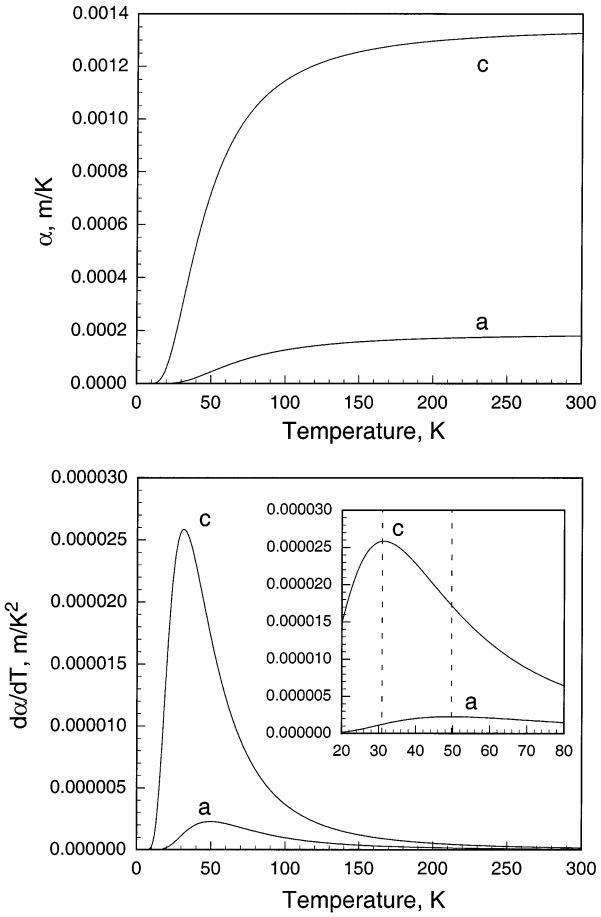

Figure 5. First and second derivatives of the fits of the temperature dependence of the *a*- and *c*-axis lattice parameters shown in Figure 4. The upper graph shows the first derivative, the lower graph shows the second derivative, and the inset is an expanded portion of the second derivative.

magnetic reflections are coincident with nuclear reflections. The integrated intensities of the pure nuclear reflections have been calculated by fitting the peaks of the 20 K paramagnetic powder diffraction profile with the PROFIT program with a Gaussian line shape. The magnetic contributions to the low-temperature reflections were then calculated by subtracting the 20 K value from the integrated intensities obtained below the Curie temperature. The weak magnetic scattering at 2.0 K is shown in Figure 6 in which the paramagnetic 20 K profile has been subtracted from the 2.0 K profile.

A comparison of the room temperature powder neutron diffraction profile with those measured at low temperature shows that there is no symmetry-breaking phase transition between 300 and 2 K. However, there is considerable *Q*-dependent diffuse scattering at higher temperatures due to incoherent scattering from the thermal motion of the disordered d_{20}-PPh_4^+ cations, which is reduced at low temperature. However, the absence of a symmetry-breaking phase transition precludes the existence of complete cation ordering at low temperature.

Integrated intensities of the magnetic contributions to the powder neutron diffraction profile are listed in Table 6. The magnetic reflections are broad and weak and do not have either a Gaussian or a Lorentzian peak shape as would be expected for a completely ordered structure. Magnetic

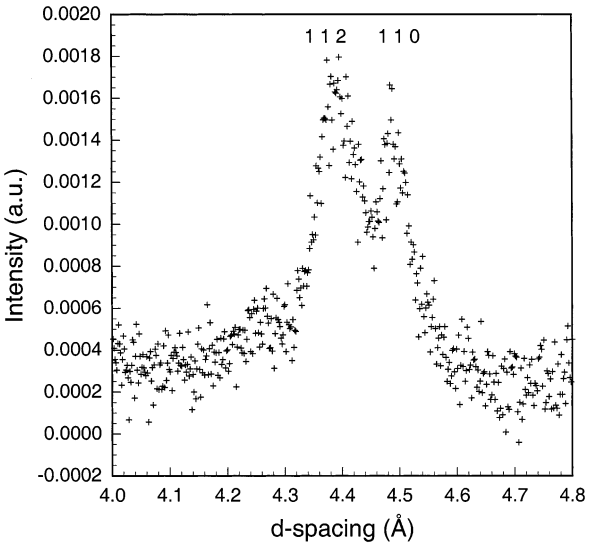

Figure 6. The magnetic scattering obtained from the difference between the 2.0 K magnetic and the 20 K paramagnetic powder neutron diffraction profiles of d_{20}-$PPh_4[FeCr(C_2S_2O_2)_3]$ measured on OSIRIS.

Table 6. Integrated Intensities (au) of the Magnetic Reflections of d_{20}-$PPh_4[FeCr(C_2S_2O_2)_3]$ Measured on GEM

T, K	110	112
2.0	0.74(5)	0.56(6)
4.0	0.35(5)	0.26(5)
6.0	0.28(5)	0.20(5)
7.0	0.04(5)	0.16(6)
8.0	0.02(5)	0.00(5)

diffraction of this type has been observed in $PPh_4[FeFe(C_2O_4)_3]$ in which the correlation length increases sharply on approaching the magnetic transition temperature but does not diverge to infinity.[19]

Magnetic Characterization. All the $A[FeCr(C_2S_2O_2)_3]$ compounds display a sharp increase in the bulk magnetization between 6 and 10 K, at which point the field-cooled and zero-field-cooled magnetizations diverge, illustrated for $NBu_4FeCr(C_2S_2O_2)_3$ in Figure 7. This divergence indicates ferromagnetic nearest neighbor magnetic exchange with Curie temperatures between 6 and 10 K. The fit of the temperature dependence of the magnetic susceptibility in the paramagnetic phase above 100 K indicates Curie−Weiss behavior with a Weiss temperature, θ, of ca. +10 K for each compound. The Curie temperatures for the corresponding oxalate compounds are ca. +12 K with a θ value of ca. +18.2 K. The magnetic parameters obtained from 0.01 T field-cooled measurements are given in Table 7.

Both the Curie temperatures and the Weiss constants observed in this study are lower than those reported[6] previously for the $N(n\text{-}C_3H_7)_4^+$ compounds, although the values of the room temperature effective magnetic moment, μ_{eff}, and the maximum value of μ_{eff} at low temperature are almost identical with those in the earlier report. Also, the similarity of the magnetic parameters obtained for the paramagnetic phase suggests that the differences may arise from the higher field (0.01 T herein vs 0.005 T in the previous work) and the different temperature ranges fitted

(19) Nuttall, C. J.; Day, P. *Inorg. Chem.* **1998**, *37*, 3885.

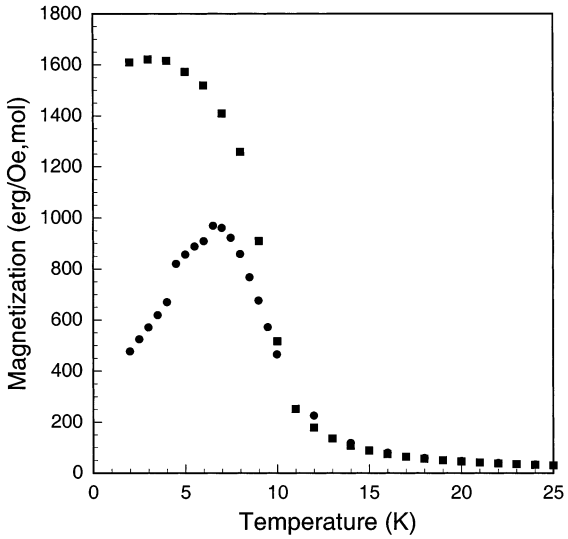

Figure 7. Low-temperature magnetization of $N(n\text{-}C_4H_9)_4[FeCr(C_2S_2O_2)_3]$ in an applied field of 100 Oe after cooling in zero-field, ●, and 100 Oe, ■.

Table 7. Magnetic Parameters of $A[MCr(C_2S_2O_2)_3]$

M^{II}	A^+	T_c, K	θ, K	C, erg Oe^{-2} mol^{-1} K	μ_{eff}, μ_B at 300 K	M_{100}, erg Oe^{-1} mol^{-1} at 2 K[a]
Fe^{II}	$N(n\text{-}C_3H_7)_4^+$	6	+10.7	5.1	6.51	1411
	$N(n\text{-}C_4H_9)_4^+$	10	+10.2	4.9	6.03	1610
	$N(n\text{-}C_5H_{11})_4^+$	8	+10.2	4.9	6.04	1600
	PPh_4^+	6	+10.4	5.2	6.59	2522
Co^{II}	$N(n\text{-}C_3H_7)_4^+$	12	+13.5	6.75	7.56	1012
	$N(n\text{-}C_4H_9)_4^+$	12	+13.0	7.17	7.78	581
	PPh_4^+	11	+12.5	6.12	7.17	483
Ni^{II}	$N(n\text{-}C_3H_7)_4^+$	15	+29.0	2.87	5.10	1339
	$N(n\text{-}C_4H_9)_4^+$	16	+31.0	2.59	4.84	289
	$[PPh_4]^+$	8	+20.0	1.55	3.68	607

[a] M_{100} is the magnetization at 2 K under 100 G after field cooling.

(100−300 K herein vs 70−300 K in the previous work).[6] The magnetic behavior of all the $A[FeCr(C_2S_2O_2)_3]$ compounds is similar, although the higher ordering temperatures observed for the longer chain tetraalkylammonium compounds are unexpected because the greater interlayer separation should lead to a more two-dimensional character and to a correspondingly lower three-dimensional ordering temperature. It is unlikely that this effect is due to particle size because the $N(n\text{-}C_3H_7)_4^+$ and PPh_4^+ cations are the most crystalline compounds in this series.

Magnetization isotherms were measured on $N(n\text{-}C_3H_7)_4[FeCr(C_2S_2O_2)_3]$ between −7 and 7 T, but the coercive field was too small to be observed (Figure 8). The saturation magnetization at 4.2 K and 7 T corresponds to ca. 6 μ_B per formula unit, the theoretical value being 7 μ_B. Magnetization isotherms were also recorded at 4.2, 6, 8, and 10 K (Figure 9). Even at 10 K the magnetization increases rapidly with applied field, indicating a persistence of the two-dimensional correlations above the Curie temperature of 6 K.

The magnetic behavior of the $A[MnCr(C_2S_2O_2)_3]$ compounds is unexpected because none show transitions to long-range magnetic order above 2 K. Temperature variation of the magnetic susceptibility and the inverse susceptibility for $N(n\text{-}C_3H_7)_4[MnCr(C_2S_2O_2)_3]$ is shown in Figure 10. The

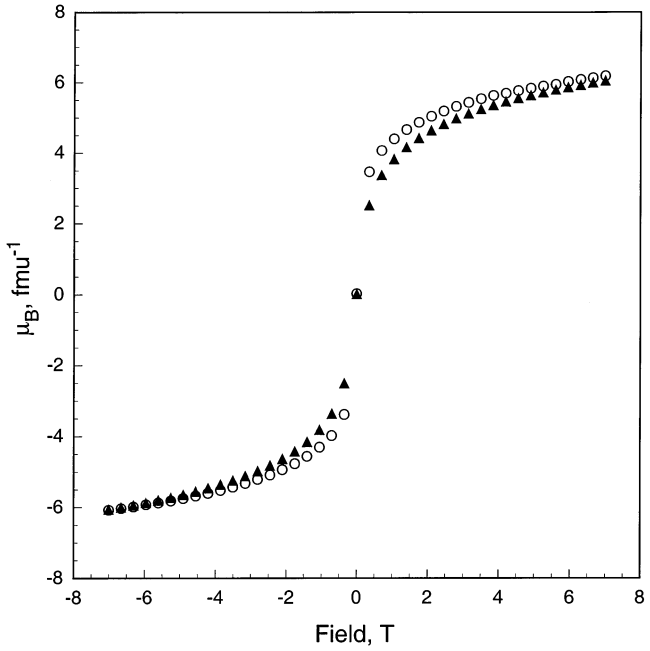

Figure 8. The magnetization of $N(n\text{-}C_3H_7)_4[FeCr(C_2S_2O_2)_3]$ at 4.2 K, ○, and 8 K, ▲.

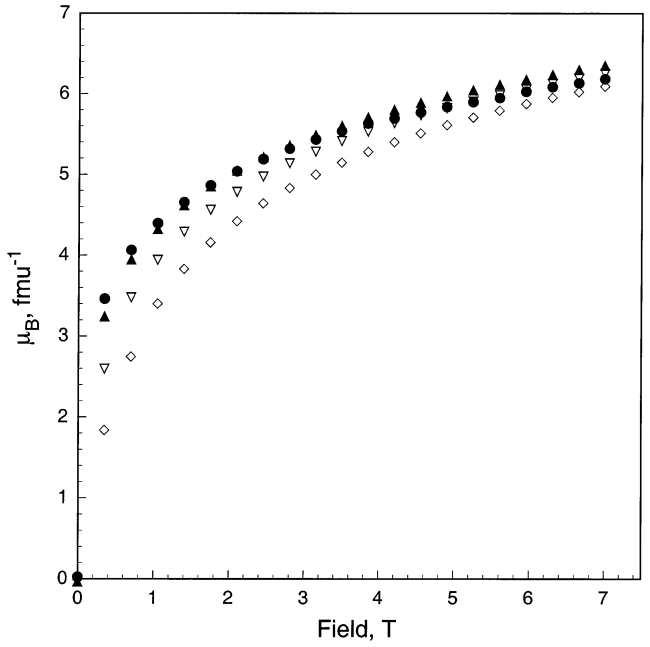

Figure 9. The magnetization of $N(n\text{-}C_3H_7)_4[FeCr(C_2S_2O_2)_3]$ at 4.2 K, ●, 6 K, ▲, 8 K, ▽, and 10 K, ◇.

negative θ contrasts with all the other $M^{II}Cr$ tris-dithiooxalates, for which the corresponding tris-oxalate compounds are ferromagnetic with T_c values of ca. 6 K and θ values of ca. +10.5 K.

The $A[CoCr(C_2S_2O_2)_3]$ and $A[NiCr(C_2S_2O_2)_3]$ compounds show T_c and θ values similar to those found for the FeCr compounds (Table 7). The low-temperature magnetization of the $N(n\text{-}C_4H_9)_4^+$ compound saturates at a much lower value than the other NiCr salts, although the other magnetic parameters are similar to those of $N(n\text{-}C_3H_7)_4[NiCr(C_2S_2O_2)_3]$. Likewise, the T_c of $PPh_4[NiCr(C_2S_2O_2)_3]$ is approximately one-half that of the two tetraalkylammonium

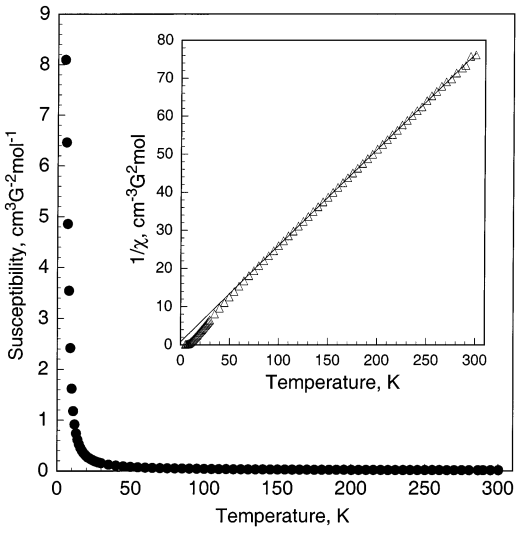

Figure 10. The temperature dependence of magnetic susceptibility and the inverse susceptibility of $N(n\text{-}C_3H_7)_4[MnCr(C_2S_2O_2)_3]$.

salts, although this compound is markedly less crystalline. The magnetic properties of the $A[CoCr(C_2S_2O_2)_3]$ compounds do not vary much with A^+ (Table 7). Figure 11a and Figure 11b show the effective magnetic moments, μ_{eff}, vs temperature for $A[NiCr(C_2S_2O_2)_3]$ and $A[CoCr(C_2S_2O_2)_3]$. The room temperature moment of $PPh_4[NiCr(C_2S_2O_2)_3]$ is much lower than the value of 6 μ_B expected for an $S_A = S_B = {}^3/_2$ system, but in no case is there a minimum in the moment, which further confirms the ferromagnetic nature of these compounds. The room temperature effective magnetic moments of the $A[CoCr(C_2S_2O_2)_3]$ series are all greater than the 5 μ_B expected for a system with $S_A = {}^3/_2$ and $S_B = 1$, presumably because of the orbital contribution to the moment of Co(II).

Mössbauer Spectral Results. The Mössbauer spectra of three samples of $PPh_4[FeCr(C_2S_2O_2)_3]$ of 1, 3, and 14 months age were fit with three symmetric quadrupole doublets. The 78 K spectra are shown in Figure 12, and the corresponding hyperfine parameters and the doublet assignments are given in Table 8.

The Mössbauer spectra clearly require three doublets for an adequate fit; two of the doublets correspond to high-spin Fe(II), and one corresponds to Fe(III). Not unexpectedly, the relatively small area of the Fe(III) doublet increases from 8.7% to 12.9% upon aging for 14 months. EXAFS studies[20] indicate that ca. 80% of the Fe(II) ions in $PPh_4[FeCr(C_2S_2O_2)_3]$ are coordinated to six dithiooxalato oxygen atoms whereas the remaining 20% of the Fe(II) ions are coordinated to four dithiooxalato oxygen atoms and two dithiooxalato sulfur atoms. The presence of the two Fe(II) coordination environments is reflected in the two Fe(II) quadrupole doublets observed in the Mössbauer spectra, the less intense of which is assigned to the O_4S_2 coordinated Fe(II) ions (Table 8). The relative areas of the three doublets indicate that the least aged sample is best formulated as $PPh_4[\{Fe_{0.77}^{II}(O_6)Fe_{0.19}^{II}(O_4S_2)Fe_{0.09}^{III}Cr_{0.93}^{III}\}(C_2S_2O_2)_3]$, where ($O_6$) and

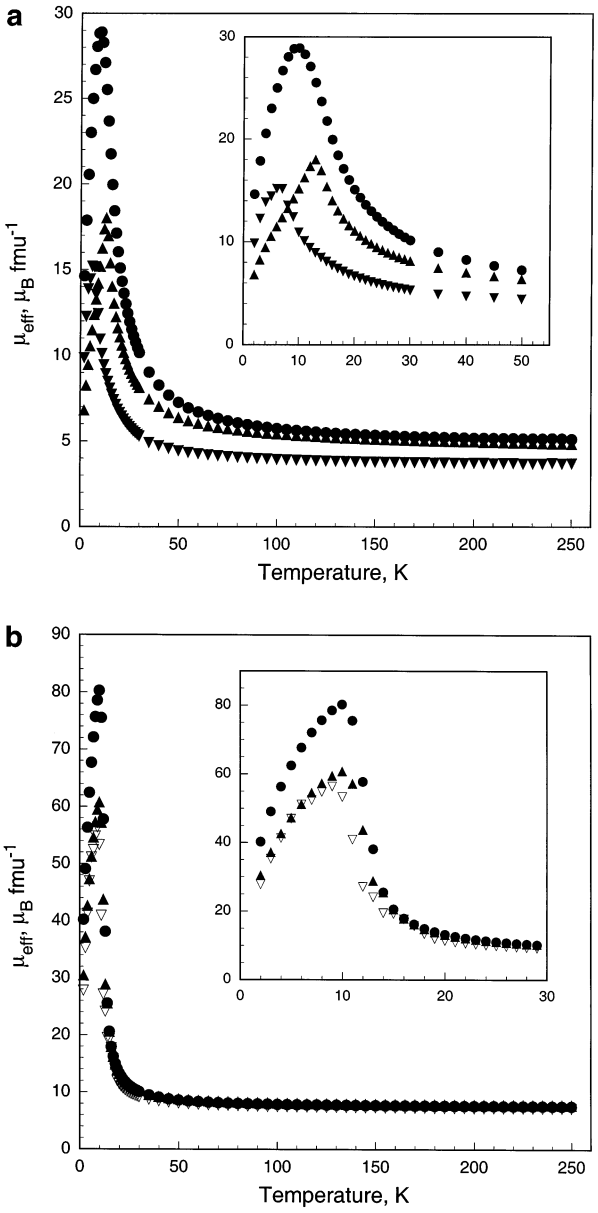

Figure 11. (a) The temperature dependence of the effective magnetic moment of $N(n\text{-}C_3H_7)_4[NiCr(C_2S_2O_2)_3]$, ●, $N(n\text{-}C_4H_9)_4[NiCr(C_2S_2O_2)_3]$, ▲, and $PPh_4[NiCr(C_2S_2O_2)_3]$, ▼. (b) The temperature dependence of the effective magnetic moment of $N(n\text{-}C_3H_7)_4[CoCr(C_2S_2O_2)_3]$, ●, $N(n\text{-}C_4H_9)_4[CoCr(C_2S_2O_2)_3]$, ▲, and $PPh_4[CoCr(C_2S_2O_2)_3]$, ▽.

(O_4S_2) indicate the respective Fe(II) coordination environments.

The Mössbauer spectra clearly indicate that the Fe(II) is high-spin whether it is bound to O_6 or O_4S_2 atoms of the coordinated $C_2S_2O_2^{2-}$ ligands. However, the hyperfine parameters of the two Fe(II) doublets do reveal differences in the bonding at these sites. Both the isomer shift and the quadrupole splitting of the O_6-bound Fe(II) ion are similar, but slightly larger, than those observed[21] in the analogous oxalato compound, $PPh_4[Fe^{II}Fe^{III}(C_2O_4)_3]$. Thus, as expected, the O_6-bound Fe(II) experience very similar electronic environments in both the oxalato and dithiooxalato com-

(20) Bradley, J. Doctoral Dissertation, University College London, 2002.

(21) Carling, S. G.; Visser, D.; Hautot, D.; Watts, I. D.; Day, P.; Ensling, J.; Gütlich, P.; Long, G. J.; Grandjean, F. *Phys. Rev. B* **2002**, *66*, 104407.

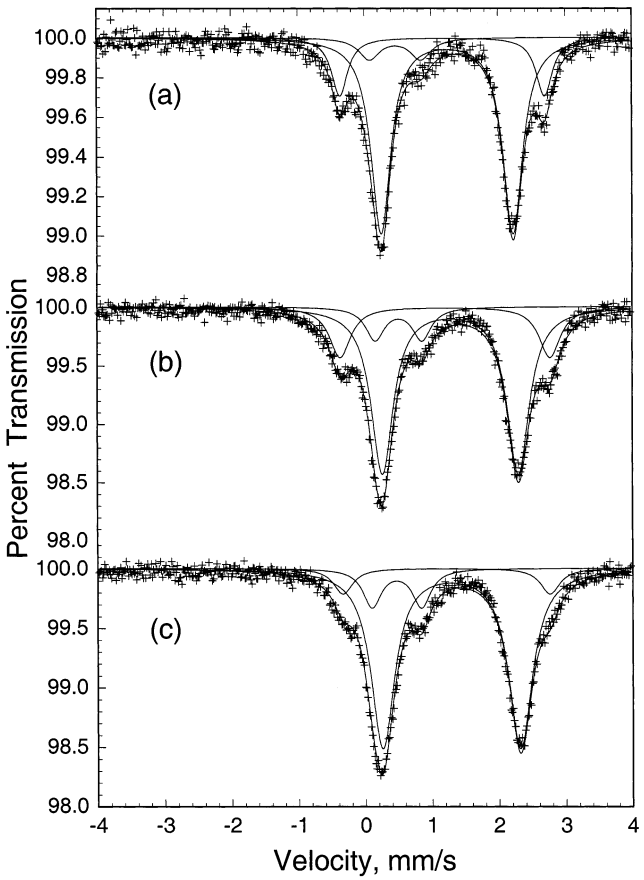

Figure 12. The Mössbauer spectra of $PPh_4[FeCr(C_2S_2O_2)_3]$ obtained at 78 K, for samples which are (a) 1 month, (b) 3 months, and (c) 14 months of age.

Table 8. Mössbauer Spectral Hyperfine Parameters for $PPh_4[FeCr(C_2S_2O_2)_3]$

age, months	*T*, K	δ, mm/s[a]	ΔE_Q, mm/s	Γ, mm/s	area, %	assignment
1	78	1.16	3.06	0.29	18.1	Fe(II) O_4S_2
		1.23	1.97	0.36	73.1	Fe(II) O_6
		0.46	0.77	0.38	8.7	Fe(III)
3	295	1.09	2.53	0.35	17.8	Fe(II) O_4S_2
		1.17	1.52	0.35	68.9	Fe(II) O_6
		0.40	0.74	0.46	13.4	Fe(III)
	78	1.20	3.14	0.38	20.0	Fe(II) O_4S_2
		1.28	2.03	0.40	68.5	Fe(II) O_6
		0.50	0.70	0.34	11.5	Fe(III)
14	78	1.21	3.10	0.35	9.2	Fe(II) O_4S_2
		1.28	2.06	0.43	77.9	Fe(II) O_6
		0.47	0.74	0.33	12.9	Fe(III)

[a] The isomer shifts are given relative to room temperature α-iron foil.

pounds. In contrast, the quadrupole splitting of ca. 3.1 mm/s observed at 78 K for the O_4S_2-bound Fe(II) in $PPh_4[FeCr(C_2S_2O_2)_3]$ is significantly larger than the 2.00 mm/s quadrupole splitting observed for O_6-bound Fe(II) in $PPh_4[Fe^{II}Fe^{III}(C_2O_4)_3]$; as expected, the O_4S_2 coordination yields a more distorted Fe(II) electronic environment.

The large increase in the Fe(II) quadrupole splittings in $PPh_4[FeCr(C_2S_2O_2)_3]$ observed upon cooling from 295 to 78 K (Table 8) is also observed[21] in $PPh_4[Fe^{II}Fe^{III}(C_2O_4)_3]$ and indicates[22] that the magnitude of the low-symmetry component of the octahedral crystal field splitting is increasing at both Fe(II) sites in $PPh_4[FeCr(C_2S_2O_2)_3]$.

The Mössbauer spectra of a variety of dithiooxalato compounds containing both high-spin and low-spin Fe(III) have been reported by Birchall and Tun.[23] The hyperfine parameters that they observe for the high-spin and low-spin Fe(III) compounds are rather similar, and, as a consequence, it is not possible to determine the spin state of the Fe(III) found in $PPh_4[FeCr(C_2S_2O_2)_3]$ from the Mössbauer data, although the parameters are somewhat more consistent with high-spin than low-spin Fe(III).

Conclusions

With the exception of Mn^{II}, all the $A[M^{II}Cr(C_2S_2O_2)_3]$ compounds are ferromagnetic with T_c values between 6 and 16 K. In contrast, the $A[MnCr(C_2S_2O_2)_3]$ compounds remain paramagnetic down to 2 K with small negative θ values. High-resolution powder X-ray diffraction data did not reveal any structural differences between ferromagnetically ordered $N(n\text{-}C_3H_7)_4[FeCr(C_2S_2O_2)_3]$ and paramagnetic $N(n\text{-}C_3H_7)_4[MnCr(C_2S_2O_2)_3]$. Furthermore, the paramagnetic behavior of the $A[MnCr(C_2S_2O_2)_3]$ compounds is not inherent to this metal combination because the corresponding oxalates are ferromagnetic with a T_c of ca. 6 K. Thus, the reason for the difference between the $Mn^{II}Cr^{III}$ oxalate and thiooxalate compounds remains unknown.

The $N(n\text{-}C_3H_7)_4[M^{II}Cr(C_2S_2O_2)_3]$ compounds reported previously[6] had higher T_c values but otherwise had magnetic parameters similar to those reported herein. In addition, the $N(n\text{-}C_4H_9)_4^+$, $N(n\text{-}C_5H_{11})_4^+$, and PPh_4^+ salts have properties similar to those based on the smaller organic cation. $N(n\text{-}C_3H_7)_4[FeCr(C_2S_2O_2)_3]$ displayed no discernible hysteresis at 4.2 K, but below the T_c value of 6 K the magnetization saturates rapidly with applied field, to a maximum value of 6.5 μ_B per formula unit at 7 T, a moment which is close to the theoretical maximum of 7 μ_B.

Powder neutron diffraction studies of d_{20}-$PPh_4[FeCr(C_2S_2O_2)_3]$ indicate that there is no structural phase transition between 2.4 and 285 K and that the coefficient of linear expansion is four times larger for the *c*-axis than for the *a*-axis because of the difference in the bonding in the two directions. In addition, the coherent magnetic scattering below T_c has a propagation vector, **q**, of zero as expected for a ferromagnet, but with an exchange correlation length which does not diverge to infinity at low temperature as was also observed for $PPh_4[FeFe(C_2O_4)_3]$.[19,21,24] In contrast to the oxalate compounds which appear to undergo ordering of the organic cations upon cooling, the PPh_4^+ in $PPh_4[FeCr(C_2S_2O_2)_3]$ remain disordered down to 1.5 K as is evidenced by the absence of any structural phase transition. This may be due to the increased void space in the honeycomb lattice of the thiooxalates.

The Mössbauer spectra of the $PPh_4[FeCr(C_2S_2O_2)_3]$ samples indicate an increasing proportion of Fe(III) from 9% to 13%

(22) Ingalls, R. *Phys. Rev.* **1964**, *133*, A787.

(23) Birchall, T.; Tun, K. M. *Inorg. Chem.* **1976**, *15*, 376.

(24) Visser, D.; Carling, S. G.; Watts, I. D.; Day, P.; Andersen, K. H. *Physica B* **1999**, *267*−*268*, 266.

over a period of 14 months. The high-spin Fe(II) is best described as two distinct sites having either O_6 or O_4S_2 coordination environments. The Fe(II) with O_6 near-neighbors has hyperfine parameters similar to those found in the related oxalates whereas the Fe(II) with O_4S_2 near-neighbors is more distorted and represents only ca. 20% of the Fe(II) contribution.

Acknowledgment. The authors thank Dr. F. Grandjean for many helpful discussions during the course of this work. This work has been supported by the UK Engineering and Physical Sciences Research Council. We are grateful to ISIS and the ILL for access to neutron beam time and to A. Hewat, T. Hansen, P. Radaelli, and K. Andersen for help with the experiments. We acknowledge the ESRF for access to synchrotron radiation and thank O. Masson for assistance with the experiment. G.J.L. thanks the "Fonds National de la Recherche Scientifique", Brussels, Belgium, for support during a sabbatical leave at the University of Liège during the 2000−2001 academic year. D.V. thanks the NWO, The Netherlands, for financial support.

Supporting Information Available: Positional parameters, description of EXAFS studies, bond lengths, temperature factors, refined parameters, and plots of EXAFS and Fourier transform data. This material is available free of charge via the Internet at http://pubs.acs.org.

IC020302X